ACS APPLIED MATERIALS & INTERFACES

Research Article

Cite This: ACS Appl. Mater. Interfaces 2019, 11, 12032−12042

www.acsami.org

Highly Conductive Paper/Textile Electrodes Using Ligand Exchange Reaction-Induced in Situ Metallic Fusion

Sungkun Kang, Donghyeon Nam, Jimin Choi, Jongkuk Ko, Donghee Kim, Cheong Hoon Kwon, June Huh, and Jinhan Cho*

Department of Chemical and Biological Engineering, Korea University, 145 Anam-ro, Seongbuk-gu, Seoul 02841, Republic of Korea

Supporting Information

ABSTRACT: Here, we report that metal nanoparticle (NP)-based paper/textile electrodes with bulk metallic conductivity can be prepared via organic linker-modulated ligand exchange reaction and in situ room-temperature metallic fusion without additional chemical or thermal treatments. For this study, amine-functionalized molecule linkers instead of bulky polymer linkers were layer-by-layer (LbL)-assembled with tetraoctylammonium bromide (TOABr)-stabilized Au NPs to form Au NP multilayered films. By conversion of the amine groups of the organic molecule linkers from $-NH_3^+$ to the $-NH_2$ groups, as well as by a decrease in the size of the organic linkers, the LbL-assembled Au NPs became highly interconnected and fused during LbL deposition, resulting in Au NP multilayers with adjustable conductivity and transport behavior. These phenomena were also predicted by a density functional theory investigation for the model system. Particularly, LbL-assembled films composed of TOABr-Au NPs and diethylenetriamine (M_w: ∼104) exhibited a remarkable electrical conductivity of 2.2×10^5 S·cm^{-1}, which was higher than the electrical conductivity of the metal NP-based electrodes as well as the carbon material-based electrodes reported to date. Furthermore, based on our approach, a variety of insulating flexible papers and textiles were successfully converted into real metal-like paper and textile electrodes with high flexibility preserving their highly porous structure. This approach can provide a basis for further improving and controlling the electrical properties of flexible electrodes through the control of organic linkers.

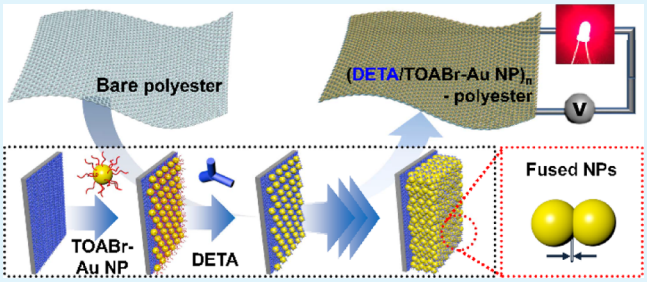

KEYWORDS: *metal nanoparticle, metallic textile, DETA ligand, metallic fusion, ligand exchange reaction, density functional theory*

INTRODUCTION

Metal nanoparticle (NP)/organic nanocomposite films, which have mainly been prepared by the self-assembly of block copolymers,[1,2] solution blending,[3−5] the Langmuir−Blodgett method,[6,7] coordination-driven assembly,[8] the seed-growth method,[9,10] or layer-by-layer (LbL) assembly,[11−17] have attracted considerable attention because of their potential use in various applications, such as biological films,[5,10] catalysts,[9] and electrically active films.[6−8,16,17] Particularly, the recent rapid progress and evolution of flexible electrodes have necessitated the development of metal NP-based films that can maintain electrical conductivity under external mechanical stimuli by minimizing the contact area between the substrate and NPs as well as by forming multiple NP layers through a high affinity between NPs and polymers.[17] Although various metal nanowires, which can form favorable conductive networks through their increased aspect ratio, have been widely used for flexible electrodes, their synthesis, separation, and mechanical stiffness have limited the applications of metal nanowire-based electrodes.[18−20] Furthermore, the presence of insulating polymeric linkers (or binders) and/or bulky organic ligands within nanocomposite electrodes seriously obstructs the electron transport between adjacent metal NPs or nanowires, resulting in high contact resistance.[21,22] These phenomena also explain why the solution-cast or spin-coated films prepared from bulky organic ligand-stabilized metal NP solutions cannot be used as conductive electrodes without additional treatments such as high-temperature sintering and/or mechanical pressing.[16,17,23−25]

Recently, an LbL assembly, which is based on complementary interactions (i.e., electrostatic, hydrogen-bonding, and covalent-bonding interactions) between two different components, has been effectively used to prepare metal or metal oxide NP-based nanocomposite films.[11−17,24−34] For example, the sequential LbL assembly of Au NPs and thiol-functionalized organics in aqueous media can generate electrically conductive films. However, directly applying thiol chemistry to various flexible substrates such as plastics, papers, or textiles is extremely difficult because of the poor affinity between their mutual interfaces. In addition, the use of electrostatically charged metal NPs generally results in NP arrays with a low packing density per layer because of the long-range electrostatic repulsion between the identically charged NPs in aqueous media,[14,27,28] which is closely related to the increase

Received: December 7, 2018
Accepted: March 6, 2019
Published: March 18, 2019

DOI: 10.1021/acsami.8b21445
ACS Appl. Mater. Interfaces 2019, 11, 12032−12042

in contact resistance. Recently, Kim et al. reported that electrostatic LbL-assembled Au NP films (i.e., 4 multistacked films with 500 bilayers per stack) composed of bulky cationic polyurethane and anionic Au NPs in aqueous media exhibited a high electrical conductivity of 1.1×10^4 S·cm^{-1} after mechanical pressing at 130 °C.[17] These previous results suggest the possibility that the electrical properties of metal NP multilayers can be strongly influenced by the packing density of metal NPs, the presence of bulky ligands, and the size of organic linkers. Therefore, unique approach allowing elaborate control over the adsorption mechanism, adsorption behavior, and electron transport within metal NP multilayers as well as the ligand exchange reaction of organic ligands bound to the surface of metal NPs can provide an effective pathway for the preparation of highly conductive and flexible electrode based on various substrates (polyester, nylon, papers, plastics, etc.).

Here, we introduce highly conductive paper/textile electrodes prepared using organic linker-modulated ligand exchange reaction and in situ room-temperature metallic fusion phenomena. We also demonstrate that the electrical conductivity of metal NP films assembled onto paper and textiles can be significantly enhanced through minute control over interaction moieties, adsorption conditions, the degree of ligand exchange, and the size of organic linkers (Scheme 1).

Scheme 1. Schematic Showing the Preparation of Highly Conductive Au NP Multilayers on Flexible Substrates Using Various NH_2-Functionalized Organic Linkers

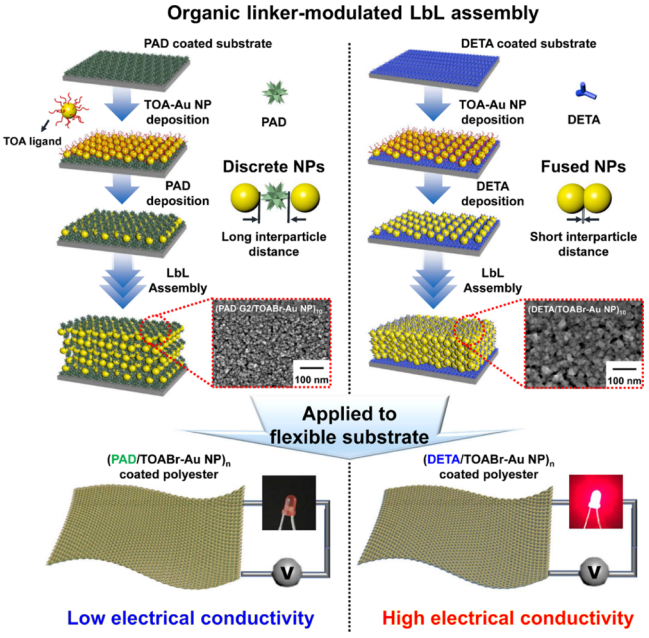

Furthermore, we demonstrate that the close interparticle distance between neighboring metal NPs induces the partial metallic fusion during metal NP assembly, which has a decisive effect on the electrical conductivity and electron transport mechanism. For this study, tetraoctylammonium bromide (TOABr)-Au NPs were sequentially LbL-assembled with various amine (NH_2)-functionalized organic linkers with different M_w values in alcohol and aqueous media. With decreasing M_w (related to the size or length scale) of the organic linkers, the electrical conductivity of the nanocomposite films increased, causing the partial metallic fusion of Au−Au NPs and a dramatic change in films' charge transport behavior from hopping to metallic conductivity. In addition, the LbL assembly of TOABr-Au NPs using the neutral NH_2-functionalized organic linkers in alcohol significantly increased the degree of ligand exchange compared with that observed from the same kind of organic linkers with electrostatic charges (i.e., $-NH_3^+$ linkers) in aqueous media, resulting in higher conductivity. We also highlight that the LbL assembly of TOABr-Au NPs and diethylenetriamine (DETA) molecule linkers with an extremely small M_w (~104) (i.e., (DETA/TOABr-Au NP)$_n$) exhibited a remarkable electrical conductivity (2.2×10^5 S·cm^{-1} for 10 bilayers) proximate to the conductivity of bulk Au (4.1×10^5 S·cm^{-1}) showing the Au mass composition of approximately 98%; such performance is possible despite a room-temperature assembly process and is superior to the conductivity of conventional metal NP films reported to date. Simulation results based on the density functional theory indicate that DETA adopts a flat conformation on the Au surface, forming a nearly atomic-scale layer between the Au surfaces with an optimal separation distance of ~7 Å. Although it has been reported that the strong metallic bonding between metal NPs can occur when the interparticle separation is less than 5 Å,[35] our results suggest that room-temperature metallic fusion of Au−Au NPs through atomic diffusion can be induced in the gap distance of 7 Å. Given that our approach can be easily and widely applied to various substrates, including thermal and/or pressure-sensitive paper, textiles, and plastics, we believe that this study provides an important basis for the development of fully flexible electrodes with bulk metal-like conductivity and textile-like mechanical properties.

MATERIALS AND METHODS

Synthesis of TOABr-Au NPs. TOABr (>98%, Alfa Aesar)-stabilized Au NPs were synthesized as previously reported.[36] First, 20 mM solution of TOABr dispersed in toluene (80 mL) and 30 mM solution of gold(III) chloride trihydrate ($HAuCl_4 \cdot 3H_2O$, ≥99.9%, Sigma-Aldrich) dispersed in deionized water (30 mL) were prepared. The TOABr solution and gold precursor solution were then mixed with vigorous stirring. After the Au precursor was sufficiently transferred into an organic medium, 0.5 M sodium borohydride ($NaBH_4$, 99.99%, Sigma-Aldrich) aqueous solution was slowly added to the mixture to chemically reduce the Au NPs, after which the mixture was further stirred for 3 h. The organic phase was subsequently separated from the aqueous solution. The synthesized TOABr-stabilized Au NP solution was washed with 0.1 M H_2SO_4 (95%, Daejung Chemicals), 0.1 M NaOH (97%, Sigma-Aldrich), and deionized water several times.

Fabrication of (Organic Linker/TOABr-Au NP) Multilayer Films. For the fabrication of the (organic linker/TOABr-Au NP) multilayer films, a quartz glass or silicon substrate was first cleaned with RCA solution (H_2O, NH_4OH, and H_2O_2 in a 5:1:1 volume ratio) at 70 °C. On the other hand, the substrates (i.e., papers, PETs, and/or textiles) containing a large amount of OH and C═O functionalities were used without additional RCA treatment because they have the hydrogen-bonding affinity with amine-functionalized organic linkers [i.e., PAD-Gm, tris(2-aminoethyl)amine (TREN), and DETA]. Additionally, the solution concentrations of all the organic linkers were adjusted to be 1 mg·mL^{-1}. In this case, the substrates were dipped into an amine-functionalized organic linker solution (in ethanol) for 10 min, then thoroughly washed twice with ethanol and dried under a gentle air stream. The organic linker-coated substrates were dipped into TOABr-Au NP solution (in toluene) for 30 min, followed by washing with toluene and drying with air. The substrates were then dipped into the organic linker solution for another 10 min. The dipping cycles were repeated until the desired number of layers was obtained.

DOI: 10.1021/acsami.8b21445
ACS Appl. Mater. Interfaces 2019, 11, 12032−12042

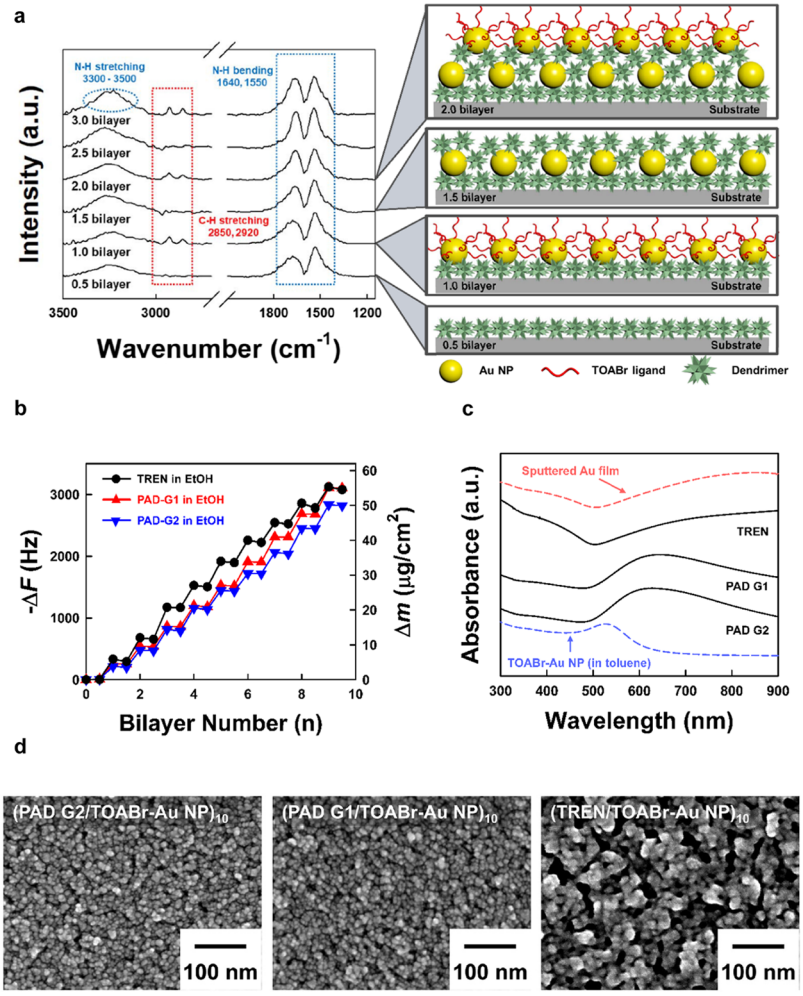

Figure 1. (a) ATR–FTIR spectra and schematic images of $(PAD\text{-}G2/TOABr\text{-}Au\ NP)_n$ multilayers as a function of the layer number (n). (b) QCM data (i.e., frequency (ΔF) and mass (Δm) changes) of $(NH_2$ organic linker/TOABr-Au NP$)_n$ as a function of the bilayer number. (c) UV–vis spectra and (d) FE-SEM images of the $(PAD\text{-}G2/TOABr\text{-}Au\ NP)_{10}$, $(PAD\text{-}G1/TOABr\text{-}Au\ NP)_{10}$, and $(TREN/TOABr\text{-}Au\ NP)_{10}$ multilayers.

Characterization. Fourier transform infrared (FTIR) spectra of the fabricated multilayer films were recorded with a CARY 600 spectrometer (Agilent Technology) operated in specular mode and with 4 cm^{-1} resolution. The spectrometer sample chamber was purged with N_2 for 1 h to remove water and CO_2 before the FTIR measurement. The collected data were analyzed with spectrum analysis software (OMNIC, Nicolet). For quantitative measurement of film growth, a quartz crystal microbalance device (QCM 200, SRS) was used. The change in adsorbed mass (Δm) was calculated from the variation in the QCM frequency (ΔF) using the Sauerbrey equation[37]

$$\Delta F(\mathrm{Hz}) = -\frac{2F_0^{\,2}}{A\sqrt{\rho_q \mu_q}} \cdot \Delta m \qquad (1)$$

where F_0 (~5 MHz) is the free resonance frequency, A is the surface area, ρ_q (~2.65 g·cm^{-2}) is the shear modulus, and μ_q (~2.95 × 10^{11} g·cm^{-2}·s^{-2}) is the density of the QCM electrode. With the aforementioned values, this equation can be simplified to

$$-\Delta F(\mathrm{Hz}) = 56.6 \times \Delta m_A \qquad (2)$$

where Δm_A is the change in adsorbed mass per unit area of the QCM electrode, with units of $\mu g \cdot cm^{-2}$. UV–vis spectra of the fabricated multilayer films on quartz glass were acquired with a Lambda 35 (PerkinElmer) spectrometer in a scan range from 200 to 1000 nm. The surface morphology [field-emission scanning electron microscopy (FE-SEM)] and elemental mapping (energy-dispersive X-ray spectroscopy) of the LbL-assembled films was investigated using an S-4800 (Hitachi) scanning electron microscope. X-ray photoelectron spectroscopy (XPS) was conducted using X-TOOL (ULVAC-PHI) equipped with an Al Kα, X-ray source (1486.6 eV, 24.1 W, 15 kV). The main chamber was maintained at a pressure less than 4.25 × 10^{-7} Pa. Binding energies were referenced to the Au $4f_{7/2}$ signal at 84.0 eV. All spectra were acquired with an analyzer pass energy of 140 eV. The temperature-dependent electrical resistance was measured by a physical property measurement system (PPMS-9, Quantum Design). Thermogravimetric analysis (TGA) for the multilayers was performed over the temperature range from 20 to 600 °C using TGA Q50 (TA Instruments).

Computational Methods. The energetics of the amine linkers (TREN and DETA) between Au(110) surfaces were computed as a function of the separation distance using a periodic density functional theory (DFT) module (BAND), as implemented in the Amsterdam Density Functional (ADF) program[38,39] with the Perdew–Burke–Ernzerhof generalized gradient approximation functional[40] and a double zeta plus polarization basis set.[41] The sandwich geometry was prepared by placing an organic linker between two Au slabs, each of which was built by face-centered-cubic stacking of 3 layers with a (110) face consisting of a 3 × 4 supercell. Geometry optimization was performed with a fixed-atom constraint for Au atoms and the scalar relativistic ZORA option.

RESULTS AND DISCUSSION

Size Effect of Organic Linkers on the Electrical Conductivity. To investigate the effect of the size of organic

DOI: 10.1021/acsami.8b21445
ACS Appl. Mater. Interfaces 2019, 11, 12032–12042

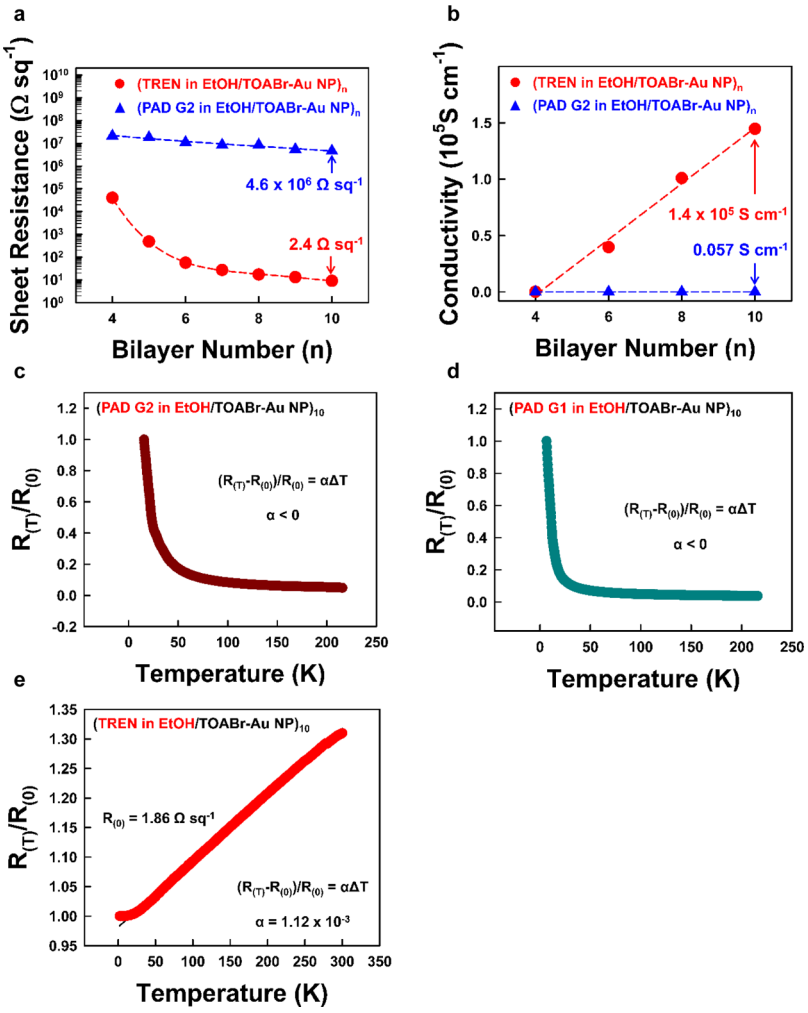

Figure 2. (a) Sheet resistance and (b) electrical conductivity of (PAD-G2/TOABr-Au NP)$_n$, (PAD-G1/TOABr-Au NP)$_n$, and (TREN/TOABr-Au NP)$_n$ as functions of the bilayer number (n). The resistance ($R_{(T)}/R_{(0)}$) vs temperature (K) of the (c) (PAD-G2/TOABr-Au NP)$_{10}$, (d) (PAD-G1/TOABr-Au NP)$_{10}$, and (e) (TREN/TOABr-Au NP)$_{10}$ multilayers coated onto quartz glass. The electrical properties of the Au NP multilayers shown in (a,b) were measured at room temperature.

linkers on the electrical conductivity of metal NP arrays, TOABr-Au NPs with a diameter of approximately 7 nm in toluene were first LbL-assembled using NH_2 organic linkers (poly(amidoamine) dendrimers with different generations (Gm) [PAD-G1, $M_w \approx 1430$ and PAD-G2, $M_w \approx 3256$] and TREN ($M_w \approx 146$)) with different M_w values and molecular structures in alcohol (Figure 1). Generally, the NH_2 groups are well known to have a high affinity toward metal surfaces such as Au, Ag, and Pt. Therefore, the bulky TOABr stabilizers loosely bonded to the surface of Au NPs could be easily replaced by the NH_2 groups of PAD via ligand exchange reaction during LbL deposition.[14,15,31,42−46] When the TOABr-Au NPs were deposited onto PAD-G2-coated substrates, the bulky TOABr stabilizers bonded to the bottom surface of the Au NPs were replaced by the NH_2 groups of PAD-G2. Although TOABr ligands bound to the top surface of the Au NPs have no affinity with PAD-G2, the successive deposition of PAD-G2 onto the top of TOABr-Au NPs can induce the replacement of the remaining TOABr stabilizers by PAD-G2. These phenomena were clearly confirmed by FTIR spectroscopy in attenuated total reflection (ATR) mode (Figure 1a) and additionally were observed in PAD with different generations (i.e., PAD-G1 with $M_w \approx 1430$) and the amine-functionalized TREN with different molecular structures (Supporting Information, Figure S1). That is, the C−H stretching peaks originating from the long alkyl chains of the remaining TOABr ligands at 2850−2920 cm^{-1} disappeared after the deposition of PAD-G2. However, the additional deposition of TOABr-Au NPs onto the outermost PAD-G2 layer-coated substrates regenerated the C−H stretching peaks of the TOABr ligands. This generation and disappearance of the C−H stretching peaks (at 2850−2920 cm^{-1}) was repeated when the outermost layer was changed from PAD-G2 to TOABr-Au NPs and vice versa.[47,48] Notably, the organics sandwiched between adjacent Au NP layers is mainly single organic layers such as PAD-Gm or TREN. On the basis of this LbL assembly, the film thickness and the loading amount of (TREN/TOABr-Au NP)$_n$, (PAD-G1/TOABr-Au NP)$_n$, and (PAD-G2/TOABr-Au NP)$_n$ multilayers with an increasing bilayer number (n) to 9.5 were quantitatively measured using cross-sectional FE-SEM (Supporting Information, Figure S2) and a QCM (Figure 1b). Although the total film thickness of the (TREN/TOABr-Au NP)$_{10}$ multilayer (approximately 29 nm in thickness) was smaller than that of (PAD-Gm/TOABr-Au NP)$_{10}$ (approximately 37−38 nm in thickness) (Supporting Information, Figure S2), and the loading amount (i.e.,

DOI: 10.1021/acsami.8b21445
ACS Appl. Mater. Interfaces 2019, 11, 12032−12042

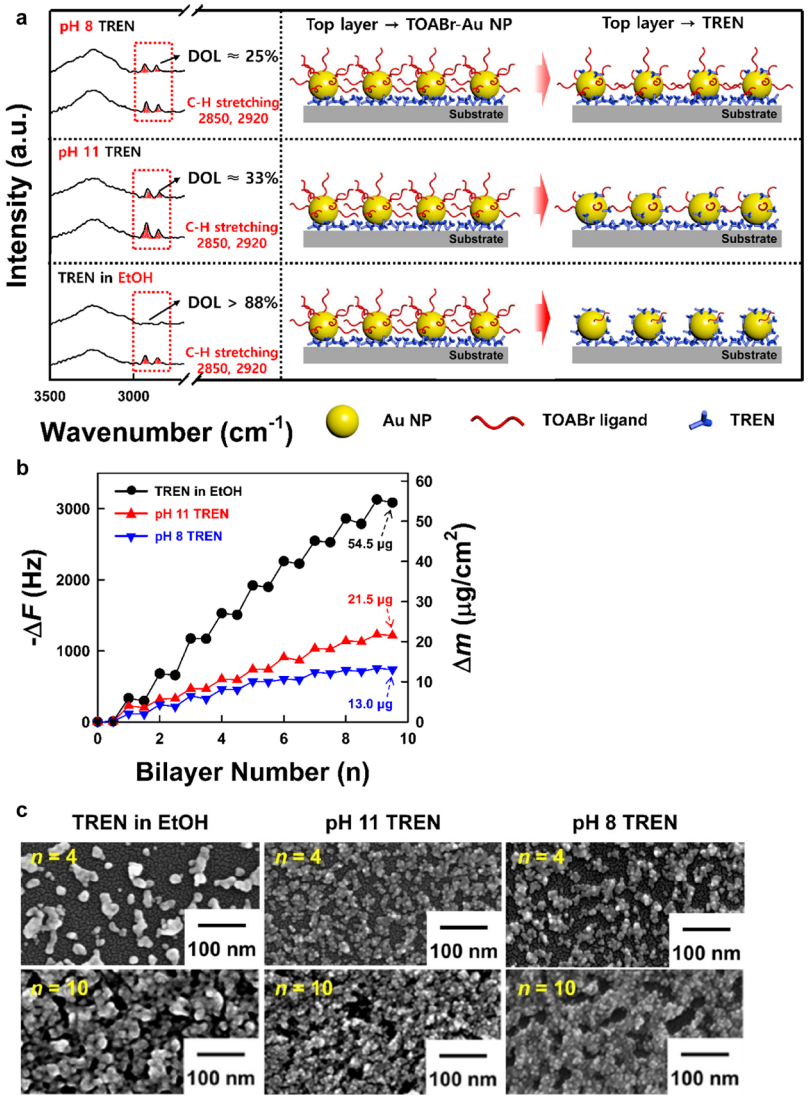

Figure 3. (a) ATR−FTIR spectra of (pH 8 TREN/TOABr-Au NP)$_{n=1,1.5}$, (pH 11 TREN/TOABr-Au NP)$_{n=1,1.5}$, and (TREN in ethanol/TOABr-Au NP)$_{n=1,1.5}$ multilayers. In this case, the degree of ligand exchange was calculated using the integrated absorbance area of the C−H stretching peaks. The schematic shows the ligand exchange LbL assembly. (b) QCM data of (cationic TREN in water/TOABr-Au NP)$_n$ and (TREN in ethanol/TOABr-Au NP)$_n$ multilayers as functions of the bilayer number (n). (c) FE-SEM images of (TREN in ethanol/TOABr-Au NP)$_{n=4,10}$, (pH 11 TREN/TOABr-Au NP)$_{n=4,10}$, and (pH 8 TREN/TOABr-Au NP)$_{n=4,10}$.

frequency changes ($-\Delta F$) of 350 ± 60 Hz and a Δm of approximately 6.2 μg·cm^{-2}) of TOABr-Au NP per layer in the (TREN/TOABr-Au NP)$_n$ multilayers was higher than that (i.e., $-\Delta F$ of 320−350 Hz and Δm of 5.7−6.2 μg·cm^{-2}) of (PAD-Gm/TOABr-Au NP)$_n$. Herein, the loading mass amount (Δm) was calculated from the frequency changes ($-\Delta F$) of the QCM (see Materials and Methods section). Additionally, when the TREN/TOABr-Au NP multilayers were thermally annealed at 600 °C, the mass ratio of Au NPs embedded within the multilayers was measured to be approximately 98.1% by TGA (the latter part will be explained). The dependence of NH_2 linkers on the loading amount of TOABr-Au NPs was confirmed by the atomic ratio analysis of (NH_2 linker/TOABr-Au NP)$_{10}$ multilayer films (without thermal treatment) by XPS (Supporting Information, Figure S3).[49,50] The atomic ratio of the respective components was converted to the mass ratio of components using their atomic mass. In this case, the mass ratios of Au NPs within the TREN/TOABr-Au NP, the PAD-G1/TOABr-Au NP, and the PAD-G1/TOABr-Au NP multilayers were measured to be 90.5, 84.0, and 84.0%, respectively. Additionally, the disparity between the Au ratio values in the (TREN/TOABr-Au NP)$_n$ multilayers obtained from TGA and XPS measurements was mainly caused by the amount of thermally decomposed TREN and TOABr. These results imply that adsorbed TREN, despite its small M_w, can produce many more binding sites with TOABr-Au NPs than can relatively bulky PAD-G1 and PAD-G2 and can thereby increase the loading density of Au NPs per layer. Furthermore, these results imply that TREN linkers can significantly decrease the interparticle distance between neighboring Au NPs to a significantly greater degree than PAD-G1 or PAD-G2.

To demonstrate this possibility, we investigated the change in the surface plasmon resonance spectra of (NH_2 linker/TOABr-Au NP)$_n$ multilayers using UV−vis spectroscopy. With decreasing M_w of NH_2 linkers (i.e., from PAD-G2 to TREN) for the LbL assembly of TOABr-Au NPs, the surface plasmon resonance absorption peak of the Au NP multilayers gradually

DOI: 10.1021/acsami.8b21445
ACS Appl. Mater. Interfaces 2019, 11, 12032−12042

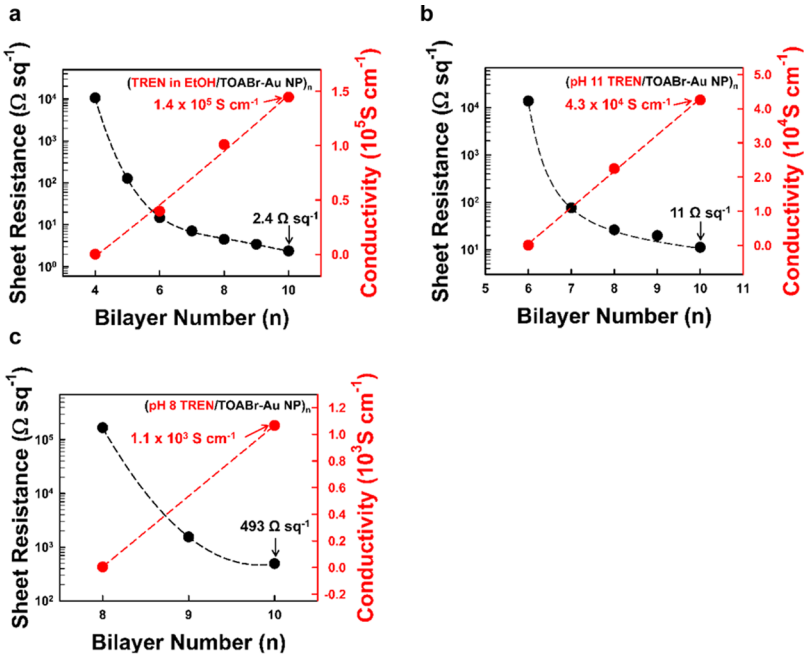

Figure 4. Sheet resistance and electrical conductivity of (a) (TREN in ethanol/TOABr-Au NP)$_n$, (b) (pH 11 TREN/TOABr-Au NP)$_n$, and (c) (pH 8 TREN/TOABr-Au NP)$_n$ multilayers as functions of the bilayer number (n).

broadened and red-shifted, indicating the formation of more closely packed Au NP arrays (Figure 1c, and Supporting Information, Figure S4).[51] In the case of the (TREN/TOABr-Au NP)$_{10}$ multilayer, the plasmon absorption peak of the Au NPs was almost completely absent, similar to that of a bulk Au film. These phenomena can be more easily understood by the difference between the surface morphologies of the (TREN/TOABr-Au NP)$_{10}$ and (PAD-G1 or PAD-G2/TOABr-Au NP)$_{10}$ multilayers (Figure 1d). That is, the (TREN/TOABr-Au NP)$_{10}$ film exhibited a surface morphology with a partially fused structure without distinct interfaces between neighboring TOABr-Au NPs; by contrast, the (PAD-G1 or PAD-G2/TOABr-Au NP)$_{10}$ film still displayed a morphology with discrete and spherical Au NPs.

In line with the surface morphology, we examined the electrical properties of the (NH_2 linker/TOABr-Au NP)$_n$ multilayers with an increasing bilayer number (n) from 4 to 10 (Figure 2a,b). First, the electrical conductivity of the (PAD-G2/TOABr-Au NP)$_{10}$ multilayer was measured to be approximately 0.057 S·cm^{-1} (sheet resistance of ~4.6 × 10^6 Ω·sq^{-1}). Although the electrical conductivity of (PAD-Gm/TOABr-Au NP)$_n$ could be further increased by decreasing the generation (Gm) of PAD and/or by increasing n, the increase in conductivity was limited. This change of electrical conductivity according to the size of organic linkers was also confirmed by the use of bulky poly(ethylene imine) linkers (M_w ≈ 800 and 25 000) bridging between neighboring Au NPs (Supporting Information, Figure S5). However, in the case of (TREN/TOABr-Au NP)$_n$ multilayers with partially fused structures, during LbL assembly, their electrical conductivity and sheet resistance were significantly enhanced to 1.1 × 10^5 S·cm^{-1} and reversely lowered to 2.4 Ω·sq^{-1} as n was increased to 10. These results strongly imply that M_w of the organic linker related to the interparticle distance strongly affects the electrical conductivity of the LbL-assembled Au NP multilayers.

Furthermore, to investigate the electron transport mechanism of the (PAD-Gm/TOABr-Au NP)$_n$ and (TREN/TOABr-Au NP)$_n$ multilayers, we obtained the temperature-dependent electrical resistance by four-probe measurement in the temperature range from 2 to 300 K for (TREN/TOABr-Au NP)$_n$ multilayers and from 2 to 220 K for PAD-Gm/TOABr-Au NP)$_n$ multilayers (Figure 2c–e, and Supporting Information, Figure S6). First, in the case of the (PAD-G2/TOABr-Au NP)$_n$ multilayers, the electrical conductivity as a function of temperature exhibited a linear dependence (as a plot of ln σ vs $K^{-1/2}$) with the following hopping conduction equation: $\sigma = \sigma_0 \exp(-A/T^{1/2})$, where σ is the conductivity, T is the absolute temperature (K), and A is a constant. This hopping conduction behavior was also observed in the (PAD-G1/TOABr-Au NP)$_n$ multilayers (Supporting Information, Figure S6). However, the (TREN/TOABr-Au NP)$_n$ multilayers with minimized interparticle distance exhibited metallic conduction behavior instead of hopping conduction.[52] That is, as the temperature was decreased from 300 to 2 K, the electrical resistivity of the (TREN/TOABr-Au NP)$_{10}$ multilayer linearly decreased, demonstrating typical metallic conduction behavior. In this case, the TREN-based multilayers showed a positive temperature coefficient of 1.12 × 10^{-3} K^{-1}, which is characteristic of a pure metal, as obtained by the equation $\Delta R_T/R_0 = \alpha \Delta T$, where ΔR_T (i.e., $(R_T - R_0)/R_0$, where R_T and R_0 are resistances at temperatures T and 2 K, respectively) and α are the resistance (Ω) and the temperature coefficient, respectively. As a result, the size of the organic linker bridging neighboring Au NP layers governs the electron transport mechanism.

Effect of Charged Amine Groups on the Electrical Conductivity. We also examined the relationship between the type of the primary amine group in the organic linker and the electrical conductivity of the Au NP multilayers. For this study, pH-controlled TREN aqueous solutions (from pH 8 to 11) were prepared for the LbL assembly of TOABr-Au NPs in toluene. Generally, the NH_2 group, with a pK_a of ~10 (more specifically, "pK_a" indicates the pH at which 50% of functional

DOI: 10.1021/acsami.8b21445
ACS Appl. Mater. Interfaces 2019, 11, 12032–12042

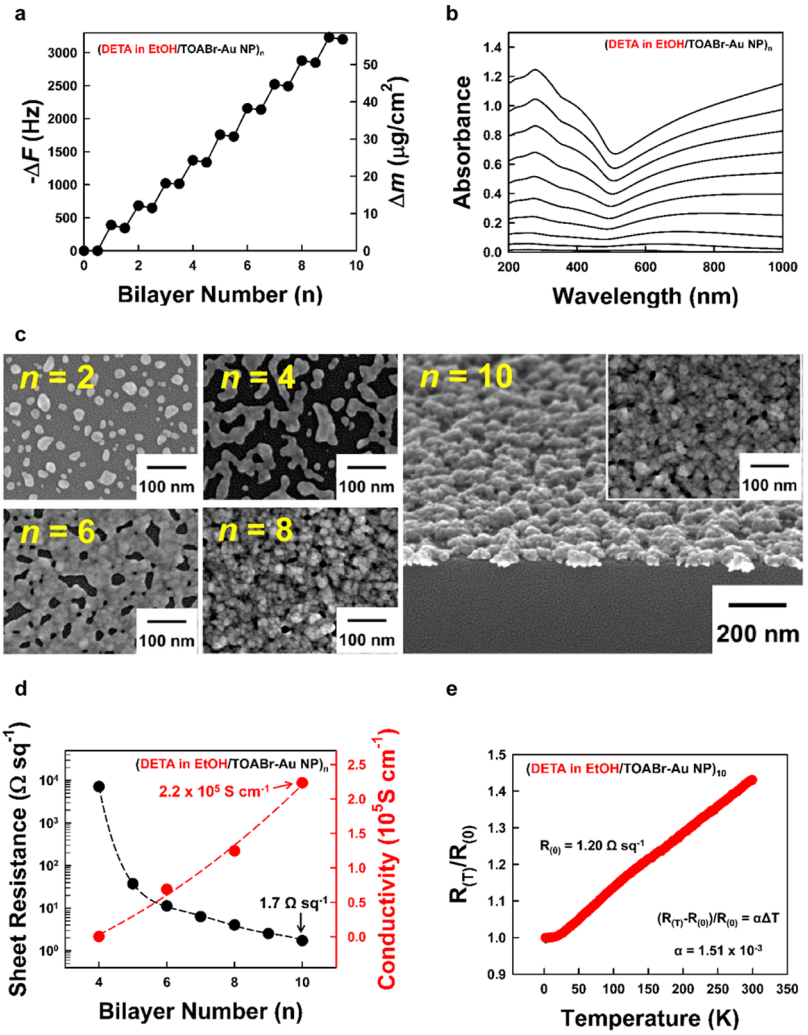

Figure 5. (a) QCM measurement data, (b) UV−vis spectra, and (c) FE-SEM images of $(DETA/TOABr\text{-}Au\ NP)_n$ as functions of the bilayer number (n). (d) Electrical conductivity and sheet resistance of $(DETA/TOABr\text{-}Au\ NP)_n$ as functions of the bilayer number (n). In this case, the electrical properties of the Au NP multilayers were measured at room temperature. (e) Resistance ($R_{(T)}/R_{(0)}$) vs temperature (K) of $(DETA/TOABr\text{-}Au\ NP)_{10}$ multilayers coated onto quartz glass.

groups, such as NH_2 moieties, are ionized), is easily converted into a protonated amine group (NH_3^+) at low pH and into a neutral amine group at high pH. According to a previous report,[53] when the solution pH decreases from 11 to 5, the degree of ionization of the NH_2 group increases from approximately 5−96%. First, the degrees of the ligand exchange reaction in the $(pH\ 8\ TREN/TOABr\text{-}Au\ NP)_n$ and $(pH\ 11\ TREN/TOABr\text{-}Au\ NP)_n$ multilayers were measured to be approximately 25 and 33%, respectively, as confirmed by FTIR spectroscopy (Figure 3a and Supporting Information, Figure S7) (herein, the "degree of ligand exchange reaction" was calculated by comparing the absorbance peak area of the TOABr group with long alkyl chains at 2850−2950 cm^{-1} before and after the adsorption of TREN onto the TOABr-Au NP layer by spectroscopy). These results are in stark contrast with the degree of ligand exchange reaction of above 88% shown in the $(TREN\ in\ ethanol/TOABr\text{-}Au\ NP)_n$ multilayers. The low ligand exchange reaction obtained from the $(cationic\ TREN/TOABr\text{-}Au\ NP)_n$ multilayers suggests that a relatively large amount of residual TOABr ligands bonded to the surface of Au NPs can restrict the formation of an effective electron transport pathway among neighboring Au NPs and additionally induce a high contact resistance through the low loading of Au NPs per layer. For further confirming these possibilities, the adsorbed amount of TOABr-Au NPs and TREN was quantitatively measured by a QCM during LbL assembly (Figure 3b). The total adsorbed amount of the $(TREN\ in\ ethanol/TOABr\text{-}Au\ NP)_{9.5}$ multilayer was measured to be approximately 54.5 $\mu g \cdot cm^{-2}$, which was almost a twofold increase over that of the $(pH\ 11\ TREN/TOABr\text{-}Au\ NP)_{9.5}$ multilayer. Additionally, the metallic fused structure formed during sequential LbL assembly was more clearly observed in $(TREN\ in\ ethanol/TOABr\text{-}Au\ NP)_n$ than in the $(cationic\ TREN/TOABr\text{-}Au\ NP)_n$ multilayers (Figure 3c and Supporting Information, Figure S8).

Furthermore, these phenomena (i.e., the adsorbed amount of Au NPs, degree of ligand exchange reaction, and metallic fusion) directly affected the electrical conductivity of the TOABr-Au NP multilayers. As shown in Figure 4, when TREN was changed from neutral to cationic, the electrical conductivities of the resultant $(cationic\ TREN/TOABr\text{-}Au\ NP)_n$ multilayers were significantly decreased; however, their sheet resistance values were notably increased, although the electron transport of the cationic TREN-based films was still

DOI: 10.1021/acsami.8b21445
ACS Appl. Mater. Interfaces 2019, 11, 12032−12042

based on metallic conduction behavior (Supporting Information, Figure S9). These results imply that a large amount of residual TOABr ligands on the surface of Au NPs within the (cationic TREN/TOABr-Au NP)$_n$ multilayers interrupt the decrease in the interparticle distance related to the metallic fusion and resultantly induce the formation of a limited pathway for electron transport. However, in the case of preparing LbL multilayers composed of citrate ion-stabilized Au NPs (i.e., anionic Au NPs) and cationic pH 11 TREN, these films did not exhibit electrical conductivity because the electrostatic repulsion between the identically charged Au NPs generates the extremely low surface coverage of anionic Au NPs (i.e., high contact resistance).

Enhancement of Electrical Conductivity. Based on the intimate relationship between electrical conductivity and organic linkers, we sought to design LbL-assembled Au NP multilayers with an electrical conductivity approaching that of bulk Au films. To this end, DETA, whose molecules are substantially smaller ($M_{w,DETA}$: ∼104) than TREN molecules ($M_{w,TREN}$: ∼146), was selected as the organic linker in ethanol for the buildup of TOABr-Au NP multilayers. The thicknesses of (DETA/TOABr-Au NP)$_n$ multilayers were quantitatively measured using cross-sectional FE-SEM and atomic force microscopy (Supporting Information, Figure S10). As shown in the QCM analysis, alternating the deposition of DETA and TOABr-Au NPs resulted in Δm values of approximately 6.3 $\mu g \cdot cm^{-2}$ ($-\Delta F \approx 340 \pm 30$ Hz) per TOABr-Au NP layer, which was comparable to those of the (TREN/TOABr-Au NP)$_n$ multilayers (Figure 5a). Additionally, TGA showed that the mass ratio of the Au NPs within (DETA/TOABr-Au NP)$_n$ was approximately 98.6% (the mass ratio of Au NPs within the TREN/TOABr-Au NP multilayers was ∼98.1%) (Supporting Information, Figure S11). Similar to the adsorption behavior of the (TREN in ethanol/TOABr-Au NP)$_n$ multilayers, the TOABr ligands loosely bonded to the surface of Au NPs were almost completely replaced by the neutral amine groups of DETA during LbL assembly (degree of ligand exchange >92%). When DETA was adsorbed onto the TOABr-Au NP-coated substrate, the C−H stretching peaks derived from the long alkyl chains of the TOABr ligand (at 2850−2920 cm^{-1}) disappeared from the FTIR spectrum upon the ligand exchange reaction between DETA and TOABr ligands (from 1 to 1.5 bilayers) (Supporting Information, Figure S12). However, the deposition of TOABr-Au NPs onto the outermost DETA layer regenerated the absorption peaks of TOABr ligands (from 1.5 to 2 bilayers). Therefore, the alternating deposition of DETA and TOABr-Au NPs generated inversely correlated changes in the peak intensities of the C−H stretching frequencies of TOABr ligands.

On the basis of these results, we further investigated the surface plasmon spectra of (DETA/TOABr-Au NP)$_n$ multilayers using UV−vis spectroscopy. With increasing bilayer numbers for the multilayers, the surface plasmon resonance absorption peak of the multilayers broadened and red-shifted (Figure 5b). We also investigated the surface morphology of the (DETA/TOABr-Au NP)$_n$ multilayers with increasing bilayer numbers. The DETA-based multilayers exhibited a more fused and interconnected structure than the (TREN/TOABr-Au NP)$_n$ multilayers for the same bilayer number (Figure 5c and Supporting Information, Figure S13). In particular, the electrical conductivity of the (DETA/TOABr-Au NP)$_{10}$ multilayer was measured to be approximately 2.2 × 10^5 $S \cdot cm^{-1}$ (sheet resistance of ∼1.7 $\Omega \cdot sq^{-1}$), which is nearly two times higher than that (electrical conductivity of ∼1.1 × 10^5 $S \cdot cm^{-1}$; sheet resistance of ∼2.4 $\Omega \cdot sq^{-1}$) of the (TREN/TOABr-Au NP)$_{10}$ multilayer. Additionally, it should be noted that the electrical conductivity of the (DETA/TOABr-Au NP)$_{10}$ multilayer is superior to other metal NP- or carbon-based conductive films reported to date (Supporting Information, Table S1).[2,6,17,19,54−63] These films also exhibited typical metallic conductive behavior when their electrical conductivity was measured as a function of temperature (Figure 5d,e and Supporting Information, Figure S14). These phenomena imply that the use of extremely small organic linkers such as DETA can significantly intensify the metallic fusion among Au NPs at room temperature without any additional treatments (e.g., chemical reduction or thermal annealing) and that LbL films with a bulk metal-like conductivity can be prepared from spherical-type metal NPs with a higher contact resistance than metal nanowires.

In addition, we estimated the optimal interparticle distance by a DFT investigation of a model system featuring an organic linker sandwiched between two Au surfaces, where the energetics of the organic linker were computed as a function of the separation distance between Au surfaces. The DFT results suggest that both organic linkers DETA and TREN, which adopt a flat conformation on the Au surface, form a nearly atomic-scale layer between the Au surfaces, with an optimal separation distance of ∼7 Å (Supporting Information, Figure S15).

We speculate that such a thin layer of low-M_w NH_2 linkers adhered to the Au surfaces plays an optimal role in the trade-off between metallic fusion and NP spreading. The estimated adsorption energies of the amine linkers on the single surface are 11.1 kcal/mol for TREN, which has 4 amino groups, and 8.0 kcal/mol for DETA, which has one less amino group than TREN. Interestingly, this trend of adsorption energy on the single surface becomes reversed for the linkers between Au surfaces, with adsorption energies of 31.2 kcal/mol for TREN and 37.2 kcal/mol for DETA. This reversed trend reflects greater perturbation of TREN than DETA when sandwiched between Au surfaces, which may rationalize that DETA is more effective than TREN in ligand exchange. Although it has been reported that the strong metallic bonding between metal NPs can occur when the separation distance between neighboring metal NPs is less than 5 Å,[35,64] our results also demonstrate that metallic fusion occurs in NP separation distance within 7 Å. Furthermore, we also confirmed that the electrical properties of the (DETA/TOABr-Au NP)$_{10}$ multilayer film could be well maintained under the repeated bending and peeling test, implying excellent mechanical stability (Figure 6 and Supporting Information, Figure S16).

On the basis of these results, we prepared various highly flexible and metallic electrodes through the conformal deposition of (DETA/TOABr-Au NP)$_{10}$ multilayers onto commercial A4 paper, polyester textiles, nylon, poly(ethylene terephthalate) (PET), and polyurethane rubber. As previously mentioned, these flexible metallic electrodes are difficult to prepare using conventional approaches such as thiol chemistry or electrostatic LbL assembly. As shown in Figure 7a, the (DETA/TOABr-Au NP)$_{10}$ multilayer-coated electrodes could be effectively used as metallic conductors, maintaining the intrinsic mechanical properties of their flexible substrates. Furthermore, our method can be easily applied to large-area flexible materials such as polyester, A4 paper, and so forth (Figure 7b and Supporting Information, Figure S17). As

DOI: 10.1021/acsami.8b21445
ACS Appl. Mater. Interfaces 2019, 11, 12032−12042

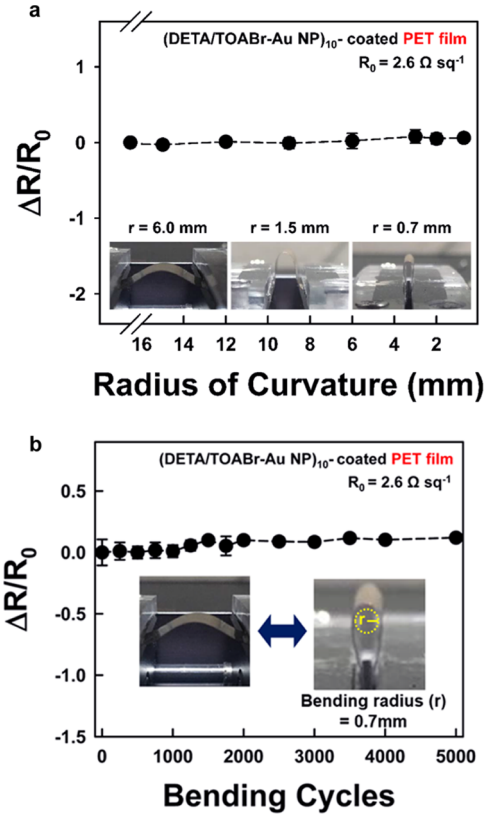

Figure 6. Resistivity change ($\Delta R/R_0$) of the (DETA/TOABr-Au NP)$_{10}$ multilayers as a function of (a) bending radius and (b) bending cycle number (bending radius (r) ≈ 0.7 mm). In this case, the initial sheet resistance (R_0) was measured to be 2.6 Ω·sq^{-1}.

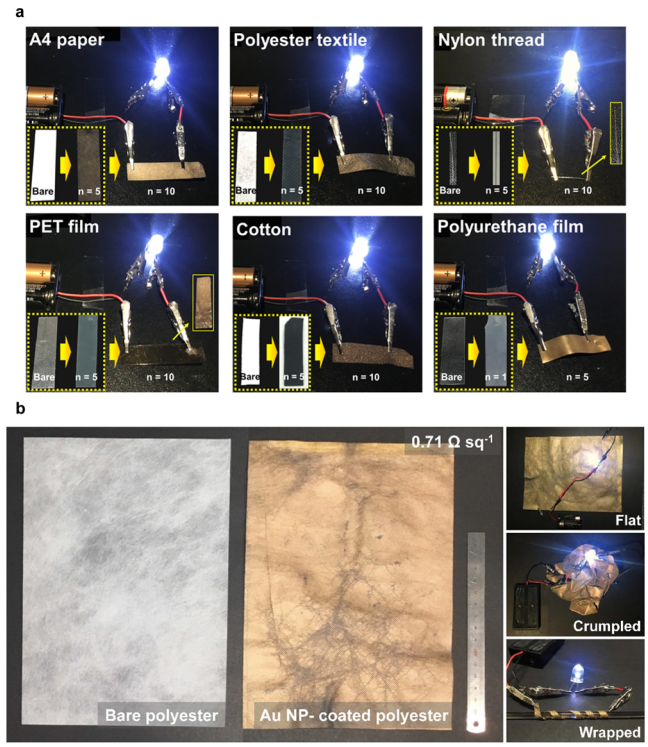

Figure 7. Photographs of (DETA/TOABr-Au NP)$_n$ multilayer-coated (a) commercial A4 paper, polyester textile, nylon, PET, cotton, and polyurethane films with a light-emitting diode connection. (b) Photographic images of the large-area (24 cm × 18 cm) polyester textile.

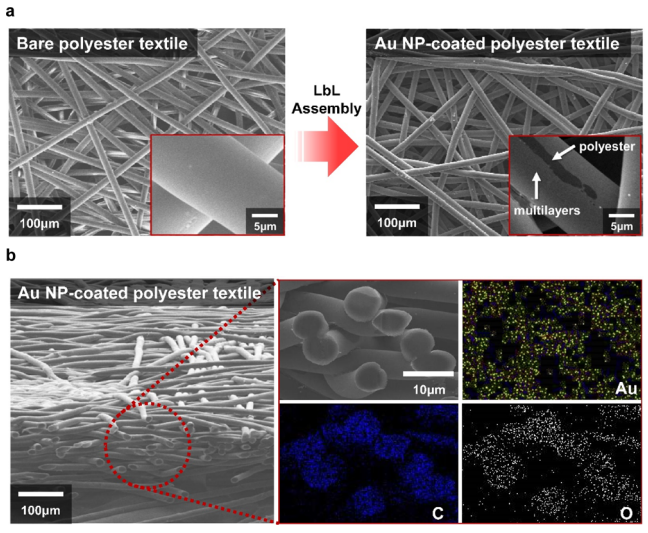

Figure 8. (a) FE-SEM images of the bare polyester textile and the (DETA/TOABr-Au NP)$_{10}$-coated polyester textile. (b) FE-SEM and elemental mapping images of (DETA/TOABr-Au NP)$_{10}$ multilayer-coated polyester textiles.

previously discussed, the electrical conductivity of these flexible electrodes could be further enhanced by increasing the bilayer number. Another remarkable feature is that, in the case of depositing the (DETA/TOABr-Au NP)$_{10}$ multilayer onto the highly porous and large-area polyester textile, the densely packed Au NP multilayers were uniformly coated over all of the polyester fibril surfaces, ranging from the interior to the exterior of the textile, without blocking the porous structure, as confirmed by elemental mapping images (Figure 8). These results clearly indicate that various templates with microporous 3D networks can be easily converted into porous metallic electrodes with a large specific surface area.

CONCLUSIONS

We demonstrated that highly flexible paper and textile with metal-like electrical conductivity could be prepared by the multilayered Au NP arrays with consecutive ligand exchange reaction and in situ metallic fusion. Particularly, the type and size of the NH_2-functionalized linkers bridging vertically adjacent metal NPs critically affected the degree of ligand exchange reaction, the metallic fusion among neighboring metal NPs, and the electrical properties of multilayers. With decreasing size of the organic linkers (i.e., from PAD-G2 to DETA), the electrical conductivity of the (NH_2 linker/TOABr-Au NP)$_n$ multilayers dramatically approached that of a bulk Au film, accompanying the metallic fusion of Au NPs; additionally, the electrical behavior changed from hopping to metallic conductivity. In particular, for the same NH_2 linker, an increase of the proportion of charged amine groups (NH_3^+) within an organic linker molecule greatly decreased the degree of ligand exchange and thus limited the effective electron transport. However, the use of DETA with 100% neutral amine groups and an extremely small M_w of 104 as an organic linker enabled the preparation of metal NP nanocomposite films with a remarkable electrical conductivity of 2.2 × 10^5 S·cm^{-1} without any additional treatments; this conductivity is greater than that of metal NP-based films reported to date. Furthermore, given that the (DETA/TOABr-Au NP)$_n$ multi-

DOI: 10.1021/acsami.8b21445
ACS Appl. Mater. Interfaces 2019, 11, 12032−12042

layers can also be uniformly deposited onto various materials irrespective of substrate size and shape, our approach can provide an important basis for developing and designing various flexible electrodes with bulk metal-like conductivity while maintaining the structural and mechanical characteristics of substrates.

■ ASSOCIATED CONTENT

Supporting Information

The Supporting Information is available free of charge on the ACS Publications website at DOI: 10.1021/acsami.8b21445.

FT-IR spectra, SEM images, XPS analysis, UV−vis spectra, temperature-dependent conductivity and resistivity measurements, and TGA data; DFT investigation of the model system; and photographic images (PDF)

■ AUTHOR INFORMATION

Corresponding Author

*E-mail: jinhan71@korea.ac.kr.

ORCID

Sungkun Kang: 0000-0002-7912-3390

Cheong Hoon Kwon: 0000-0002-9516-0669

Jinhan Cho: 0000-0002-7097-5968

Notes

The authors declare no competing financial interest.

■ ACKNOWLEDGMENTS

This work was supported by the National Research Foundation (NRF) grant funded by the Ministry of Science, ICT & Future Planning (MSIP) (2018R1A2A1A05019452; 2017R1A6A3A04003192; and 2016M3A7B4910619).

■ REFERENCES

(1) Lopes, W. A.; Jaeger, H. M. Hierarchical Self-Assembly of Metal Nanostructures on Diblock Copolymer Scaffolds. *Nature* **2001**, *414*, 735−738.

(2) Warren, S. C.; Messina, L. C.; Slaughter, L. S.; Kamperman, M.; Zhou, Q.; Gruner, S. M.; DiSalvo, F. J.; Wiesner, U. Ordered Mesoporous Materials from Metal Nanoparticle-Block Copolymer Self-Assembly. *Science* **2008**, *320*, 1748−1752.

(3) Corbierre, M. K.; Cameron, N. S.; Sutton, M.; Mochrie, S. G. J.; Lurio, L. B.; Rühm, A.; Lennox, R. B. Polymer-Stabilized Gold Nanoparticles and Their Incorporation into Polymer Matrices. *J. Am. Chem. Soc.* **2001**, *123*, 10411−10412.

(4) Park, J. H.; Lim, Y. T.; Park, O. O.; Kim, J. K.; Yu, J.-W.; Kim, Y. C. Polymer/Gold Nanoparticle Nanocomposite Light-Emitting Diodes: Enhancement of Electroluminescence Stability and Quantum Efficiency of Blue-Light-Emitting Polymers. *Chem. Mater.* **2004**, *16*, 688−692.

(5) Travan, A.; Pelillo, C.; Donati, I.; Marsich, E.; Benincasa, M.; Scarpa, T.; Semeraro, S.; Turco, G.; Gennaro, R.; Paoletti, S. Non-cytotoxic Silver Nanoparticle-Polysaccharide Nanocomposites with Antimicrobial Activity. *Biomacromolecules* **2009**, *10*, 1429−1435.

(6) Bourgoin, J.-P.; Kergueris, C.; Lefèvre, E.; Palacin, S. Langmuir-Blodgett Films of Thiol-Capped Gold Nanoclusters: Fabrication and Electrical Properties. *Thin Solid Films* **1998**, *327*−*329*, 515−519.

(7) Aleksandrovic, V.; Greshnykh, D.; Randjelovic, I.; Frömsdorf, A.; Kornowski, A.; Roth, S. V.; Klinke, C.; Weller, H. Preparation and Electrical Properties of Cobalt−Platinum Nanoparticle Monolayers Deposited by the Langmuir−Blodgett Technique. *ACS Nano* **2008**, *2*, 1123−1130.

(8) Wanunu, M.; Popovitz-Biro, R.; Cohen, H.; Vaskevich, A.; Rubinstein, I. Coordination-Based Gold Nanoparticle Layers. *J. Am. Chem. Soc.* **2005**, *127*, 9207−9215.

(9) Gao, Y.; Chen, C.-A.; Gau, H.-M.; Bailey, J. A.; Akhadov, E.; Williams, D.; Wang, H.-L. Facile Synthesis of Polyaniline-Supported Pd Nanoparticles and Their Catalytic Properties Toward Selective Hydrogenation of Alkynes and Cinnamaldehyde. *Chem. Mater.* **2008**, *20*, 2839−2844.

(10) Sawada, I.; Fachrul, R.; Ito, T.; Ohmukai, Y.; Maruyama, T.; Matsuyama, H. Development of a Hydrophilic Polymer Membrane Containing Silver Nanoparticles with Both Organic Antifouling and Antibacterial Properties. *J. Membr. Sci.* **2012**, *387*−*388*, 1−6.

(11) Decher, G. Fuzzy Nanoassemblies: Toward Layered Polymeric Multicomposites. *Science* **1997**, *277*, 1232−1237.

(12) Caruso, F.; Caruso, R. A.; Möhwald, H. Nanoengineering of Inorganic and Hybrid Sphere by Colloidal Templating. *Science* **1998**, *282*, 1111−1114.

(13) Jiang, C.; Markutsya, S.; Pikus, Y.; Tsukruk, V. V. Freely Suspended Nanocomposite Membranes as Highly Sensitive Sensors. *Nat. Mater.* **2004**, *3*, 721−728.

(14) Cho, J.; Caruso, F. Investigation of the Interactions between Ligand-Stabilized Gold Nanoparticles and Polyelectrolyte Multilayer Films. *Chem. Mater.* **2005**, *17*, 4547−4553.

(15) Ko, Y.; Kwon, M.; Bae, W. K.; Lee, B.; Lee, S. W.; Cho, J. Flexible Supercapacitor Electrodes Based on Real Metal-like Cellulose Paper. *Nat. Commun.* **2017**, *8*, 536.

(16) Musick, M. D.; Keating, C. D.; Lyon, L. A.; Botsko, S. L.; Peña, D. J.; Holliway, W. D.; McEvoy, T. M.; Richardson, J. N.; Natan, M. J. Metal Films Prepared by Stepwise Assembly. 2 Construction and Characterization of Colloidal Au and Ag Multilayers. *Chem. Mater.* **2000**, *12*, 2869−2881.

(17) Kim, Y.; Zhu, J.; Yeom, B.; Di Prima, M.; Su, X.; Kim, J.-G.; Yoo, S. J.; Uher, C.; Kotov, N. A. Stretchable Nanoparticle Conductors with Self-Organized Conductive Pathways. *Nature* **2013**, *500*, 59−63.

(18) Wu, B.; Heidelberg, A.; Boland, J. J. Mechanical Properties of Ultrahigh-Strength Gold Nanowires. *Nat. Mater.* **2005**, *4*, 525−529.

(19) De, S.; Higgins, T. M.; Lyons, P. E.; Doherty, E. M.; Nirmalraj, P. N.; Blau, W. J.; Boland, J. J.; Coleman, J. N. Silver Nanowire Networks as Flexible, Transparent, Conducting Films: Extremely High DC to Optical Conductivity Ratios. *ACS Nano* **2009**, *3*, 1767−1774.

(20) Wu, Z.; Zhang, Y.-W.; Jhon, M. H.; Gao, H.; Srolovitz, D. J. Nanowire Failure: Long = Brittle and Short = Ductile. *Nano Lett.* **2012**, *12*, 910−914.

(21) Brust, M.; Bethell, D.; Kiely, C. J.; Schiffrin, D. J. Self-Assembled Gold Nanoparticle Thin Films with Nonmetallic Optical and Electronic Properties. *Langmuir* **1998**, *14*, 5425−5429.

(22) Wuelfing, W. P.; Green, S. J.; Pietron, J. J.; Cliffel, D. E.; Murray, R. W. Electronic Conductivity of Solid-State, Mixed-Valent Monolayer-Protected Au Clusters. *J. Am. Chem. Soc.* **2000**, *122*, 11465−11472.

(23) Wessels, J. M.; Nothofer, H.-G.; Ford, W. E.; von Wrochem, F.; Scholz, F.; Vossmeyer, T.; Schroedter, A.; Weller, H.; Yasuda, A. Optical and Electrical Properties of Three-Dimensional Interlinked Gold Nanoparticle Assemblies. *J. Am. Chem. Soc.* **2004**, *126*, 3349−3356.

(24) Kotov, N. A.; Dekany, I.; Fendler, J. H. Layer-by-Layer Self-Assembly of Polyelectrolyte-Semiconductor Nanoparticle Composite Films. *J. Phys. Chem.* **1995**, *99*, 13065−13069.

(25) Wang, T. C.; Cohen, R. E.; Rubner, M. F. Metallodielectric Photonic Structures Based on Polyelectrolyte Multilayers. *Adv. Mater.* **2002**, *14*, 1534−1537.

(26) Crespo-Biel, O.; Dordi, B.; Reinhoudt, D. N.; Huskens, J. Supramolecular Layer-by-Layer Assembly: Alternating Adsorptions of Guest- and Host-Functionalized Molecules and Particles Using Multivalent Supramolecular Interactions. *J. Am. Chem. Soc.* **2005**, *127*, 7594−7600.

(27) Lee, J.-S.; Cho, J.; Lee, C.; Kim, I.; Park, J.; Kim, Y.-M.; Shin, H.; Lee, J.; Caruso, F. Layer-by-Layer Assembled Charge-Trap Memory Devices with Adjustable Electronic Properties. *Nat. Nanotechnol.* **2007**, *2*, 790−795.

(28) Krogman, K. C.; Lowery, J. L.; Zacharia, N. S.; Rutledge, G. C.; Hammond, P. T. Spraying Asymmetry into Functional Membranes Layer-by-Layer. *Nat. Mater.* **2009**, *8*, 512−518.
(29) Kim, Y.; Lee, C.; Shim, I.; Wang, D.; Cho, J. Nucleophilic Substitution Reaction Based Layer-by-Layer Growth of Superparamagnetic Nanocomposite Films with High Nonvolatile Memory Performance. *Adv. Mater.* **2010**, *22*, 5140−5144.
(30) Yanagida, S.; Nishiyama, S.; Sakamoto, K.; Fudouzi, H.; Miki, K. Formation of Uniform and High-Coverage Monolayer Colloidal Films of Midnanometer-Sized Gold Particles over the Entire Surface of 1.5-in. Substrates. *Langmuir* **2017**, *33*, 9954−9960.
(31) Ko, Y.; Baek, H.; Kim, Y.; Yoon, M.; Cho, J. Hydrophobic Nanoparticle-Based Nanocomposite Films Using in Situ Ligand Exchange Layer-by-Layer Assembly and Their Nonvolatile Memory Applications. *ACS Nano* **2013**, *7*, 143−153.
(32) Kim, D.; Kim, Y.; Cho, J. Solvent-Free Nanocomposite Colloidal Fluids with Highly Integrated and Tailored Functionalities: Rheological, Ionic Conduction, and Magneto-Optical Properties. *Chem. Mater.* **2013**, *25*, 3834−3843.
(33) Ko, Y.; Shin, D.; Koo, B.; Woo Lee, S.; Yoon, W.-S.; Cho, J. Ultrathin Supercapacitor Electrodes with High Volumetric Capacitance and Stability Using Direct Covalent-Bonding between Pseudocapacitive Nanoparticles and Conducting Materials. *Nano Energy* **2015**, *12*, 612−625.
(34) Kim, Y.; Kook, K.; Hwang, S. K.; Park, C.; Cho, J. Polymer/Perovskite-Type Nanoparticle Multilayers with Multi-Electric Properties Prepared from Ligand-Addition-Induced Layer-by-Layer Assembly. *ACS Nano* **2014**, *8*, 2419−2430.
(35) Israelachvili, J. N. *Intermolecular and Surface Forces*, 3rd ed.; Academic Press: New York, 2011; pp 253−289.
(36) Brust, M.; Schiffrin, D. J.; Bethell, D.; Kiely, C. J. Novel Gold-Dithiol Nano-Networks with Non-Metallic Electronic Properties. *Adv. Mater.* **1995**, *7*, 795−797.
(37) Buttry, D. A. *Advanced in Electroanalytical Chemistry: Applications of the QCM to Electrochemistry*; Marcel Dekker Inc.: New York, 1991.
(38) te Velde, G.; Baerends, E. J. Precise Density-Functional Method for Periodic Structures. *Phys. Rev. B: Condens. Matter Mater. Phys.* **1991**, *44*, 7888−7903.
(39) te Velde, G.; Bickelhaupt, F. M.; Baerends, E. J.; Fonseca Guerra, C.; van Gisbergen, S. J. A.; Snijders, J. G.; Ziegler, T. Chemistry with ADF. *J. Comput. Chem.* **2001**, *22*, 931−967.
(40) Perdew, J. P.; Burke, K.; Ernzerhof, M. Generalized Gradient Approximation Made Simple. *Phys. Rev. Lett.* **1996**, *77*, 3865−3868.
(41) van Lenthe, E.; Baerends, E. J. Optimized Slater-Type Basis Sets for the Elements 1-118. *J. Comput. Chem.* **2003**, *24*, 1142−1156.
(42) Yoon, M.; Choi, J.; Cho, J. Multifunctional Colloids with Reversible Phase Transfer between Organic and Aqueous Media *via* Layer-by-Layer Assembly. *Chem. Mater.* **2013**, *25*, 1735−1743.
(43) Cho, I.; Kim, B. J.; Ryu, S. W.; Cho, J. H.; Cho, J. Transistor Memory Devices with Large Memory Windows, Using Multi-Stacking of Densely Packed, Hydrophobic Charge Trapping Metal Nanoparticle Array. *Nanotechnology* **2014**, *25*, 505604.
(44) Park, M.; Kim, Y.; Ko, Y.; Cheong, S.; Ryu, S. W.; Cho, J. Amphiphilic Layer-by-Layer Assembly Overcoming Solvent Polarity between Aqueous and Nonpolar Media. *J. Am. Chem. Soc.* **2014**, *136*, 17213−17223.
(45) Shin, D.; Ko, Y.; Cho, J. Layer-by-Layer Assembled (High-Energy Carbon Nanotube/ Conductive Carbon Nanotube)$_n$ Nanocomposites for High Volumetric Capacitance Supercapacitor Electrodes. *RSC Adv.* **2016**, *6*, 21844.
(46) Cheong, S.; Kim, J.-K.; Cho, J. Functional Nanocomposites with Perfect Nanoblending between Water-Soluble Polymers and Hydrophobic Inorganic Nanoparticles: Applications to Electric-Stimuli-Responsive Films. *Nanoscale* **2016**, *8*, 18315.
(47) Nam, D.; Heo, Y.; Cheong, S.; Ko, Y.; Cho, J. Amphiphilic Ligand Exchange Reaction-Induced Supercapacitor Electrodes with High Volumetric and Scalable Areal Capacitance. *Appl. Surf. Sci.* **2018**, *440*, 730−740.
(48) Bellami, L. J. *The Infrared Spectra of Complex Molecules*; Wiley: New York, 1975; pp 123−126.
(49) Nakamoto, K. *Infrared and Raman Spectra of Inorganic and Coordination Compounds*; Wiley: New York, 2008; pp 213−217.
(50) Devia, A.; Castillo, H. A.; Benavides, V. J.; Arango, Y. C.; Quintero, J. H. Growth and Characterization of AuN Films through the Pulsed Arc Technique. *Mater. Charact.* **2008**, *59*, 105−107.
(51) Ghosh, S. K.; Pal, T. Interparticle Coupling Effect on the Surface Plasmon Resonance of Gold Nanoparticles: From Theory to Applications. *Chem. Rev.* **2007**, *107*, 4797−4862.
(52) Zabet-Khosousi, A.; Dhirani, A.-A. Charge Transport in Nanoparticle Assemblies. *Chem. Rev.* **2008**, *108*, 4072−4124.
(53) Choi, J.; Rubner, M. F. Influence of the Degree of Ionization on Weak Polyelectrolyte Multilayer Assembly. *Macromolecules* **2005**, *38*, 116−124.
(54) Wang, X.; Hu, H.; Shen, Y.; Zhou, X. Stretchable Conductors with Ultrahigh Tensile Strain and Stable Metallic Conductance Enabled by Prestrained Polyelectrolyte Nanoplatforms. *Adv. Mater.* **2011**, *23*, 3090−3094.
(55) Yang, Y.; Huang, Q.; Payne, G. F.; Sun, R.; Wang, X. A Highly Conductive, Pliable and Foldable Cu/Cellulose Paper Electrode Enabled by Controlled Deposition of Copper Nanoparticles. *Nanoscale* **2019**, *11*, 725−732.
(56) Matsuhisa, N.; Kaltenbrunner, M.; Yokota, T.; Jinno, H.; Kuribara, K.; Sekitani, T.; Someya, T. Printable Elastic Conductors with a High Conductivity for Electronic Textile Applications. *Nat. Commun.* **2015**, *6*, 7461.
(57) Joo, S.-J.; Park, S.-H.; Moon, C.-J.; Kim, H.-S. A Highly Reliable Copper Nanowire/Nanoparticle Ink Pattern with High Conductivity on Flexible Substrate Prepared *via* a Flash Light-Sintering Technique. *ACS Appl. Mater. Interfaces* **2015**, *7*, 5674−5684.
(58) Zhang, C. J.; Anasori, B.; Seral-Ascaso, A.; Park, S.-H.; McEvoy, N.; Shmeliov, A.; Duesberg, G. S.; Coleman, J. N.; Gogotsi, Y.; Nicolosi, V. Transparent, Flexible, and Conductive 2D Titanium Carbide (MXene) Films with High Volumetric Capacitance. *Adv. Mater.* **2017**, *29*, 1702678.
(59) Sekitani, T.; Noguchi, Y.; Hata, K.; Fukushima, T.; Aida, T.; Someya, T. A Rubberlike Stretchable Active Matrix Using Elastic Conductors. *Science* **2008**, *321*, 1468−1472.
(60) Kim, K. S.; Zhao, Y.; Jang, H.; Lee, S. Y.; Kim, J. M.; Kim, K. S.; Ahn, J.-H.; Kim, P.; Choi, J.-Y.; Hong, B. H. Large-Scale Pattern Growth of Graphene Films for Stretchable Transparent Electrodes. *Nature* **2009**, *457*, 706−710.
(61) Shin, M. K.; Oh, J.; Lima, M.; Kozlov, M. E.; Kim, S. J.; Baughman, R. H. Elastomeric Conductive Composites Based on Carbon Nanotube Forests. *Adv. Mater.* **2010**, *22*, 2663−2667.
(62) Hu, L.; Pasta, M.; La Mantia, F.; Cui, L.; Jeong, S.; Deshazer, H. D.; Choi, J. W.; Han, S. M.; Cui, Y. Stretchable, Porous, and Conductive Energy Textiles. *Nano Lett.* **2010**, *10*, 708−714.
(63) Bae, S.; Kim, H.; Lee, Y.; Xu, X.; Park, J.-S.; Zheng, Y.; Balakrishnan, J.; Lei, T.; Ri Kim, H.; Song, Y. I.; Kim, Y.-J.; Kim, K. S.; Özyilmaz, B.; Ahn, J.-H.; Hong, B. H.; Iijima, S. Roll-to-Roll Production of 30-inch Graphene Films for Transparent Electrodes. *Nat. Nanotechnol.* **2010**, *5*, 574−578.
(64) Korgel, B. A.; Fullam, S.; Connolly, S.; Fitzmaurice, D. Assembly and Self-Organization of Silver Nanocrystal Superlattices: Ordered "Soft Spheres". *J. Phys. Chem. B* **1998**, *102*, 8379−8388.

DOI: 10.1021/acsami.8b21445
ACS Appl. Mater. Interfaces 2019, 11, 12032−12042